27th Symposium on Naval Hydrodynamics
Seoul, Korea, 5-10 October 2008

Coupled Wind-Wave Prediction for Ship Motion

Lian Shen, Di Yang (Johns Hopkins University, USA)
Dick K.P. Yue (Massachusetts Institute Technology, USA)

ABSTRACT

We develop a coupled wave-wind simulation capability for naval applications. The objective is to provide more comprehensive environmental input for ship motions and loads. Of particular interest is the effect of the presence of realistic ocean waves on the wind field and hence wind forcing, and, to a lesser extent, short-range effects of the wind field on the waves. The combined wind-wave problem is here considered in a fully dynamically coupled context for the first time. For the dynamic evolution of the wavefield, a high-order spectral (HOS) method is employed that captures all the essential nonlinear processes with the wave phase resolved. Turbulent wind motions are computed by large-eddy simulation (LES) with the precise sea surface geometry and velocity directly provided by the wave simulation. The full dynamical coupling of the two parts of the problem is achieved by feeding the high-resolution wind pressure result from LES to HOS wave simulation as wind input to obtain wind-wave growth, which then serves as the dynamically evolving boundary condition for the wind LES.

Study of winds over JONSWAP wavefields and plane progressive waves shows strong coupling between the wave and the wind, of which the two-way interaction must be taken into account in considering wind loads and sea loads for ship motions. Through a series of systematic simulations and mechanistic studies, we are able to identify key coherent structures in the wind-wave field, which is found to play an important role in the momentum transport and have immediate implications for wind load on superstructures of ships. Together with multiscale modeling and data assimilation, this work paves the way for a prediction tool that is capable of providing sufficiently large scale and realistic wind and wave field input for ship motion design and analysis.

INTRODUCTION

The accurate prediction of ocean wave and wind fields is of vital importance to naval applications. Sea load and wind load directly affect motions and structural loads as well as maneuvering of surface ships. For naval operations such as vehicle launch and recovery, aircraft landing and taking-off, and ship cargo transfer in severe weather, there is a critical need for the prediction of wind and wave fields with sufficient accuracy and resolution.

Existing prediction tools on marine atmospheric boundary layer and wavefield generally do not consider the dynamic coupling between wind and wave motions. They often treat the problem in a phase-averaged statistical framework without wave phase information, and they usually do not connect the large scales of remote sensing and meteorological modeling to small scales at which ship operates. As a result, conventional computational tools provide only coarse-grid averaged information on the wind and wave fields in the vicinity of the ship.

This state-of-art, however, has recently seen substantial opportunities for rapid advancements made possible by the latest research progress on nonlinear wavefield simulation and turbulence-wave interaction modeling and simulation. Some notable developments include: (i) deterministic phase-resolved simulation of large-scale nonlinear wavefield evolution based on a high order spectral (HOS) method (Wu, Liu and Yue 2005; Dommermuth and Yue 1985;); (ii) highly accurate turbulence simulation for flows over complex moving wavy boundaries (Sullivan, McWilliams and Moeng 2000; Shen et al. 2003); (iii) physics-based, advanced subgrid scale (SGS) models for LES and large wave simulation (LWS) of turbulence-wave interactions (Dimas and Fialkowski 2000; Shen and Yue 2001; Shen 2007); and (iv) multiscale downscaling and upscaling modeling with advanced data statistics and assimilation techniques to extract high-resolution flow field at regions of interest from large-scale observation data (Shen and Yue 2006; Liu, Shen and Yue 2008). In the present work, we aim to integrate and extend the above advancements to develop a multiscale, truly-coupled wind-wave interaction simulation approach, with a focus on applications of wave and wind field prediction in the context of surface ship motion and load computation.

With the aforementioned applications in mind, we perform a systematic study aiming at obtaining a fundament understanding of the physics of wind-wave interaction for the development of improved prediction tools. With the computer resources provided by the DoD HPC Modernization Program, a series of simulations have been performed that cover a wide range of wind and wave parameters including wind speed, wave spectrum, wave amplitude, wave age, wave nonlinearity, and wind drift. The extensive dataset obtained from direct numerical simulation (DNS) and LES provides a basis for the study of wind-wave interaction dynamics and for the development of physics-based turbulence and wave modeling.

This paper is organized as follows. We first present mathematical formulation and numerical method for simulation of turbulence over water waves. Results on turbulence statistics in winds over various plane progressive waves are first discussed. We then examine coherent vortical structures in great detail. The pressure field in the wind is further analyzed, which is essential to the wind load on ship superstructures. Finally, we present LES-HOS coupled simulation for evolution of complex broadband wavefield interacting with the wind. Conclusions of this research and some discussion on wind-wave prediction for ship motions are presented in the end.

PROBLEM DEFINITION AND NUMERICAL METHOD

We consider the three-dimensional turbulent Couette flow over a wavy boundary as shown in Figure 1. In this canonical problem, the flow is driven by a constant shear stress, τ. The Cartesian frame is fixed in space, with x, y, and z being the streamwise, spanwise, and vertical coordinates, respectively. The water wave motion can be either obtained from HOS wave simulation, or prescribed by water wave theory. For the dominant wave, a is the wave amplitude, λ the wavelength, $k = 2\pi/\lambda$ the wavenumber, and c the phase speed.

The turbulent wind motions are described by the incompressible Navier-Stokes equations

$$\frac{\partial u_i}{\partial t} + \frac{\partial (u_i u_j)}{\partial x_j} = -\frac{1}{\rho}\frac{\partial p}{\partial x_i} + \frac{1}{\mathrm{Re}}\nabla^2 u_i \tag{1}$$

$$\frac{\partial u_i}{\partial x_i} = 0 \tag{2}$$

Here u_i (i=1, 2, 3) = (u, v, w) are Cartesian velocity components in x, y, and z directions, respectively.

By applying a low-pass filter $\bar{G}(x)$ to a variable $f(x)$, we obtain the grid-scale quantity

$$\bar{f}(x) \equiv \int \bar{G}(x-x') f(x') dx', \tag{3}$$

and the subgrid-scale quantity

$$f'(x) \equiv f(x) - \bar{f}(x). \tag{4}$$

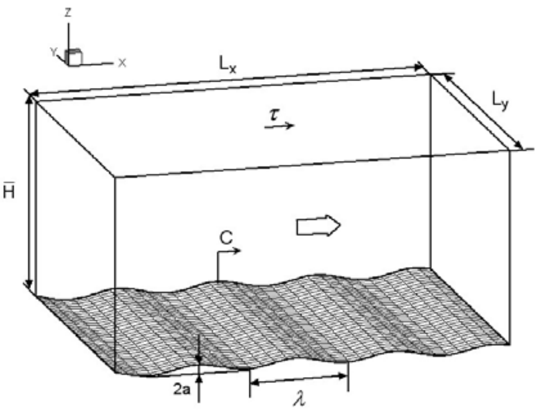

Figure 1: Sketch of a turbulent flow over water waves. The flow is driven by a shear stress τ. The dominant wave has a wavelength λ and amplitude a. The wave propagates in the x-direction with a phase speed c.

By applying the filter to equations (1) and (2), we obtain the LES governing equations for the resolved flow motions:

$$\frac{\partial \bar{u}_i}{\partial t} + \frac{\partial (\bar{u}_i \bar{u}_j)}{\partial x_j} = -\frac{1}{\rho}\frac{\partial \bar{p}}{\partial x_i} + \frac{1}{\mathrm{Re}}\nabla^2 \bar{u}_i + \frac{\partial \tau_{ij}^{\mathrm{SGS}}}{\partial x_j}, \tag{5}$$

where the last term represents the subgrid-scale effects.

As shown in Figure 2, the irregular wave-following physical space (x, y, z, t) is transformed to a rectangular computational space (ξ, ψ, ζ, τ) with the following algebraic mapping:

$$\left.\begin{aligned} \tau &= t, \\ \xi &= x, \\ \psi &= y, \\ \zeta &= \frac{z + \mathrm{H}}{\mathrm{H}} = \frac{z + \bar{\mathrm{H}} + \mathrm{H}'}{\bar{\mathrm{H}} + \mathrm{H}'}. \end{aligned}\right\} \tag{6}$$

Here the height of the physical domain H is decomposed into the average height $\bar{\mathrm{H}}$ and a wave induced variation $\mathrm{H}'(x, y, t)$. This algebraic mapping, though seemly simple in its form, is found highly efficient in our simulations of turbulent flows over complex wavefields such as high-order Stokes waves and JONSWAP wavefield.

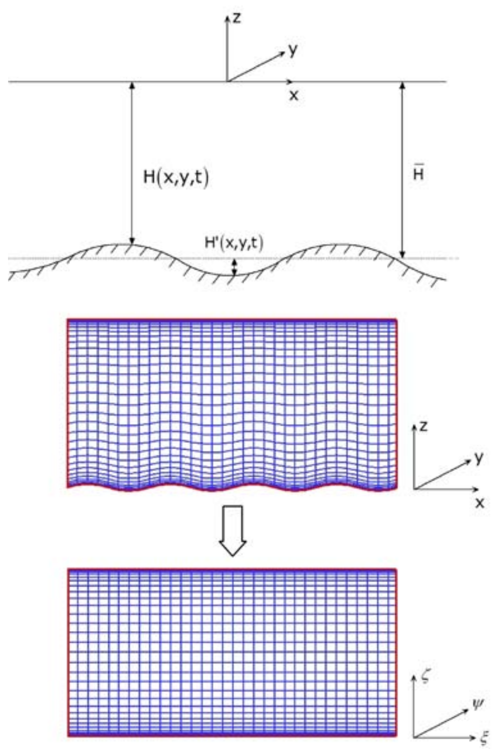

Figure 2: Illustration of algebraic mapping. The height of the physical domain H is decomposed into the average height $\overline{\mathrm{H}}$ and a wave induced variation H'. The irregular physical domain (x, y, z, t) is transformed to a rectangular computational domain (ξ, ψ, ζ, τ) with an algebraic mapping.

Note that H' is a function of x, y and t. By applying chain rule to partial differentiations, we obtain the following transform of derivatives

$$\left.\begin{aligned}
\frac{\partial}{\partial t} &= \frac{\partial}{\partial \tau} + \frac{\mathrm{H}'_t}{\overline{\mathrm{H}} + \mathrm{H}'}\frac{\partial}{\partial \zeta}, \\
\frac{\partial}{\partial x} &= \frac{\partial}{\partial \xi} + \frac{\mathrm{H}'_x}{\overline{\mathrm{H}} + \mathrm{H}'}\frac{\partial}{\partial \zeta}, \\
\frac{\partial}{\partial y} &= \frac{\partial}{\partial \psi} + \frac{\mathrm{H}'_y}{\overline{\mathrm{H}} + \mathrm{H}'}\frac{\partial}{\partial \zeta}, \\
\frac{\partial}{\partial z} &= \frac{1}{\overline{\mathrm{H}} + \mathrm{H}'}\frac{\partial}{\partial \zeta}.
\end{aligned}\right\} \tag{7}$$

By substituting the above operators into equations (1) and (2), we obtain fully nonlinear governing equations in the computational space.

For spatial discretization, we use a Fourier series based pseudo-spectral method in horizontal directions. In the vertical direction, we use a second-order finite-difference scheme on a staggered grid (Harlow and Welch 1965; Shen et al. 2003). We use an evenly distributed grid with 128 points in both streamwise and spanwise directions. In the vertical direction, we use 128 grid points that are clustered towards the bottom and top boundaries. Hereinafter, in order to simplify the formulas, we will only discuss the discretization of the general Navier-Stokes equations. The treatment of SGS terms is similar. The Navier-Stokes equation (1) and (2) are advanced in time by a fractional-step method (Kim and Moin 1985):

$$\frac{\hat{u}_\mathrm{i} - u_\mathrm{i}^\mathrm{n}}{\Delta t} = \frac{1}{2}\left(3\frac{\partial\left(u_\mathrm{i}u_\mathrm{j}\right)^\mathrm{n}}{\partial x_\mathrm{j}} - \frac{\partial\left(u_\mathrm{i}u_\mathrm{j}\right)^\mathrm{n-1}}{\partial x_\mathrm{j}}\right) + \frac{1}{2}\frac{1}{\mathrm{Re}}\nabla^2\left(\hat{u}_\mathrm{i} + u_\mathrm{i}^\mathrm{n}\right), \tag{8}$$

$$\frac{u_\mathrm{i}^\mathrm{n+1} - \hat{u}_\mathrm{i}}{\Delta t} = -\frac{\partial \phi^\mathrm{n+1}}{\partial x_\mathrm{i}}, \tag{9}$$

with

$$\frac{\partial u_\mathrm{i}^\mathrm{n+1}}{\partial x_\mathrm{i}} = 0. \tag{10}$$

Here the superscript represents the time step, and the hat represents the variables at the intermediate step of the fractional-step method. The scalar ϕ is related to pressure by the following equation

$$p^\mathrm{n+1/2} = \phi^\mathrm{n+1} - \frac{\Delta t}{2\,\mathrm{Re}}\nabla^2\phi^\mathrm{n+1}. \tag{11}$$

This scalar ϕ, called pseudo-pressure, is obtained by solving the Poisson equation

$$\frac{\partial}{\partial x_\mathrm{i}}\left(\frac{\partial \phi^\mathrm{n+1}}{\partial x_\mathrm{i}}\right) = -\frac{1}{\Delta t}\frac{\partial \hat{u}_\mathrm{i}}{\partial x_\mathrm{i}}, \tag{12}$$

which is obtained by applying the divergence operator to equation (9) and then substituting (10) into it. It is noted that after the algebraic mapping, the Laplacian operators in equations (8) and (12) become nonlinear. With the pseudo-spectral method in horizontal directions, these equations are solved iteratively.

COUPLING OF WAVE COMPUTATION AND TURBULENCE SIMULATION

For the nonlinear wavefield evolution, an efficacious high-order spectral (HOS) method makes it possible to capture all of the essential nonlinear wave interaction processes at a reasonable computational cost. The HOS approach is a pseudo-spectral method based on the Zakharov formulation (Zakharov 1968) and mode-coupling that was developed by Dommermuth and Yue (1987). It accounts for nonlinear wave interactions up to an arbitrary order M in wave steepness. By taking advantage of fast Fourier transforms (FFT), this method requires a computational cost almost linearly proportional to M and the number of wave modes N. More importantly, it achieves an exponential convergence rate of the solution with respect to both M and N for moderately steep wavefields.

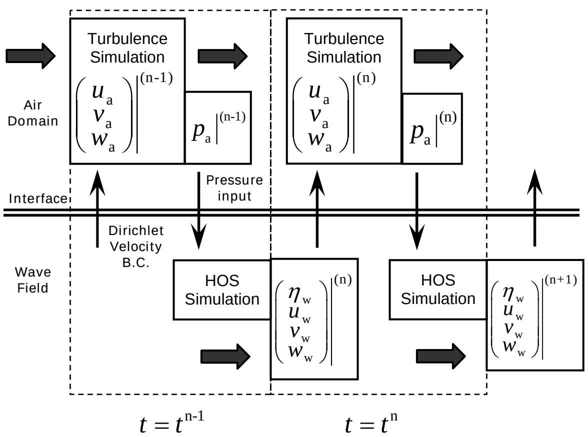

Figure 3: Schematics of turbulence-wave coupling in the simulation.

Due to space limitation, equations of the HOS method are not given here. Details of its implementation can be found in Dommermuth and Yue (1987). Complete review of the HOS method is provided in Mei et al. (2005) in their Chapter 15. The dynamic free-surface boundary condition for wave simulation is given as

$$\Phi_t^S + g\eta + \frac{1}{2}\nabla_h \Phi^S \cdot \nabla_h \Phi^S - \frac{1}{2}\left(1 + \nabla_h \eta \cdot \nabla_h \eta\right)\Phi_z^2\left(x, y, \eta, t\right) = -p_a, \tag{13}$$

where η is the displacement of the wave surface from the mean water level, p_a is the air pressure acting on the wave surface, Φ is the velocity potential, Φ^S is the potential on the free surface that is defined as

$$\Phi^S\left(x, y, t\right) = \Phi\left(x, y, \eta\left(x, y, t\right), t\right). \tag{14}$$

The Dirichlet boundary condition from surface wave motions for the simulation of wind turbulence is obtained by

$$\bar{u}\left(x, y, \eta\left(x, y, t\right), t\right) = \nabla\Phi\left(x, y, \eta\left(x, y, t\right), t\right). \tag{15}$$

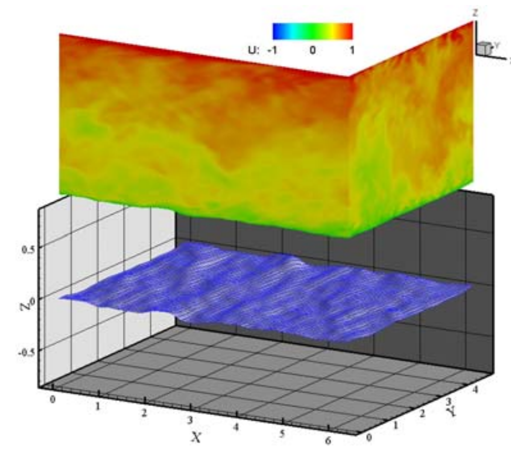

Figure 4: Wind over a JONSWAP wavefield. Surface wave profile is demonstrated by the computational mesh. In the wind field, contours of streamwise velocity component are shown on the two vertical walls. The air domain is lifted up for better visualization.

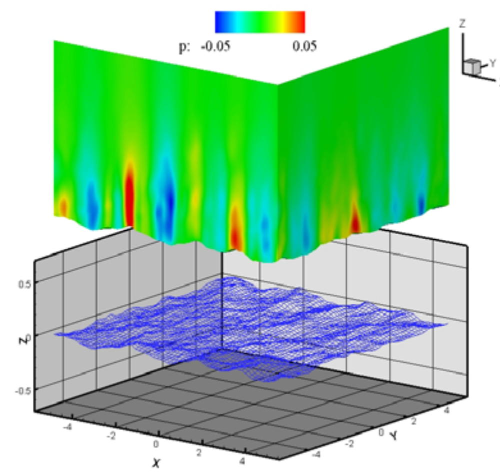

Figure 5: Wind over a JONSWAP wavefield. Surface wave profile is demonstrated by the computational mesh. In the wind field, pressure contours are shown on the two vertical walls. The air domain is lifted up for better visualization.

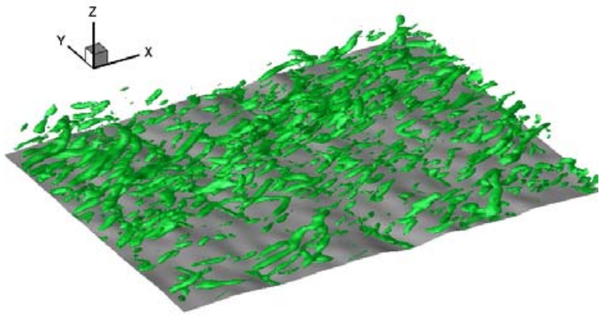

Figure 6: Snapshot of instantaneous coherent vortices in the wind over a JONSWAP wavefield.

With the surface boundary conditions (13) and (15), the wind-wave coupling system can be solved iteratively during each time step. Such an iteration approach, however, is computationally expensive, especially for the current simulation of wind turbulence with complex wavy interface that already involves iterative solver for momentum equations and pressure Poisson equation. Instead, as shown in Figure 3, an alternative fractional-step scheme is used in the present study, and the procedure is described as follows:

(1) At time step n-1: both turbulence field and wavefield have been solved.

(2) At time step n:

  (a) By using pressure of air turbulence p_a^{n-1} at time step n-1 in boundary condition (13), HOS simulation is advanced to time step n.

  (b) Surface displacement and velocities of the wave (equation (15)) at time step n are given as Dirichlet boundary conditions to airside motions, and the turbulence simulation is advanced to time step n.

(3) Proceed to time step n+1…

This alternating advancing scheme is in fact a special case of the general iterative scheme in the limit of only one iteration per timestep. As pointed out by Lombardi et al. (1996), with the small time step value that is limited by the Courant condition in the simulation of turbulence, accuracy and numerical stability in the iteration is not a concern. Our convergence test shows that a reduction in the timestep by a factor of 2 has negligible effect on both the instantaneous and statistical features of the turbulence.

Figures 4 to 6 show typical snapshots of the instantaneous turbulent wind field over the wavefield simulated by HOS. The irregular waves are obtained from an HOS simulation of a JONSWAP wavefield (Hasselmann et al. 1973). Besides the wave surface geometry, Figures 4 and 5 show respectively instantaneous velocity and pressure in the wind field, while Figure 6 shows coherent vortices in the wind. Wave-coherent turbulence structures in the wind are clearly seen. Organized quasi-streamwise and horseshoe shaped vortices are also evident. Detailed discussion on the flow structures is given in the following sections.

MECHANISTIC STUDY OF TURBULENCE STATISTICS FOR WIND OVER PLANE PROGRESSIVE WAVES

We first perform a mechanistic study on the dynamics of wind-wave interaction by a series of simulations with a wide range of water wave conditions. This systematic approach allows us to investigate the influence on wind turbulence by different wave motions including wind speed, wave steepness and nonlinearity, surface drift etc. We also investigate effect of wave age, which is defined as the ratio between the phase speed of the wave and the friction velocity of the wind turbulence. Some parameters investigated in our simulations are listed in Table 1. Due to space limitation, only representative cases are discussed in this paper. Following Belcher and Hunt (1998), we use the wave age c/u*=2 to represent young (slow) waves, c/u*=14 for intermediate waves, and c/u*=25 for mature (fast) waves.

For wind turbulence statistics, because of the boundary-fitted grid system we used in the present study, we define the phase average of a function $f(x(\mathrm{i}), y(\mathrm{j}), z(\mathrm{k}), t(\mathrm{n}))$ as

$$\langle f(x,z)\rangle \equiv \frac{1}{\mathrm{Nt}\times\mathrm{Ny}}\sum_{\mathrm{n}=1}^{\mathrm{Nt}}\sum_{\mathrm{j}=1}^{\mathrm{Ny}} f(x+ct(\mathrm{n}),y(\mathrm{j}),z(\mathrm{k}),t(\mathrm{n})), \qquad (16)$$

where the indices i, j, k, n are for discrete grid points in x, y, z, and t respectively, and Ny, Nt are the total numbers of sample points in y and t, respectively. Fluctuations are defined as $f' \equiv f - \langle f \rangle$.

Table 1: Parameters of wavy boundaries used for wind-wave simulations. Wave steepness is defined as product of wavenumber k and wave amplitude a. Wave age is defined as the ratio between the wave phase speed c and the wind turbulence friction velocity u*. Stationary wall cases are used for comparison.

Wave Steepness (ka)	0.1				0.25			
Wave Age (c/u*)	0	2	14	25	0	2	14	25
Stationary Wall	*				*			
Water Wave		*	*	*		*	*	*

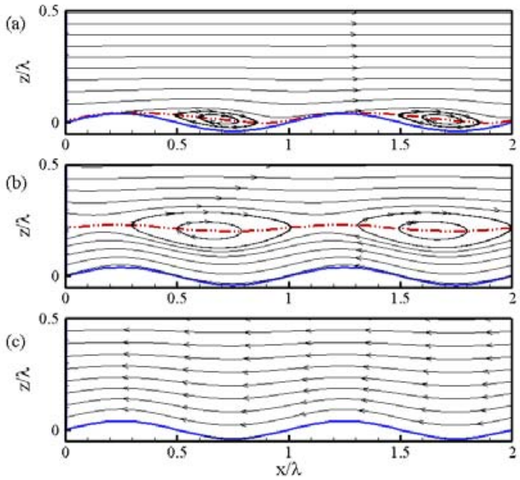

Figure 7: Phase-averaged streamline patterns over plane progressive waves with steepness ka=0.25 and various wave ages: (a) c/u*=2; (b) c/u*=14; (c) c/u*=25. Velocity used for calculating streamlines is in the wave-following frame, i.e. ($\langle u-c\rangle,\langle w\rangle$) is used in the plots. The blue curves represent wave surface. The red dash-dot-dot lines represent the height of critical layer where $\langle u-c\rangle=0$.

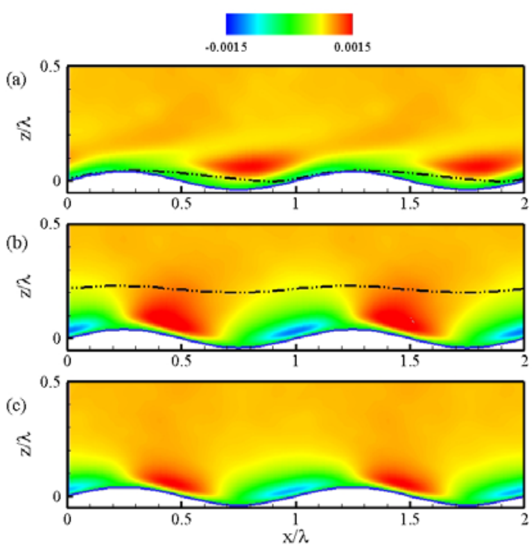

Figure 8: Contour of Reynolds stress $\langle -u'w'\rangle$ over plane progressive waves with steepness ka=0.25 and wave ages: (a) c/u*=2; (b) c/u*=14; (c) c/u*=25. The dash-dot-dot lines represent the location of the critical layer.

Figure 7 shows the phase-averaged streamline patterns for various wave ages. The height of the critical layer (Miles 1957), where the mean velocity of turbulence matches the phase speed of the wave, is also plotted as dash-dot-dot lines. In the frame traveling with the wave, the critical layer is surrounded by closed streamlines, known as the famous “cat’s-eyes” (Lighthill 1962). As we can see, for the case of c/u*=2, the critical layer lies very close to the wave surface, and it touches the surface near the crest; for the c/u*=14 case, the critical layer lies well above the wave surface and the mean flow reverses below the critical layer; for the case c/u*=25, the critical layer is located far away from the wave surface, resulting in negligible dynamical effect on the wave.

In a turbulence boundary layer, the distribution of Reynolds stress $\langle -u'w'\rangle$ is important to turbulence production and transport. In the problem of turbulence over water waves, distribution of Reynolds stress is found quite different from flat wall cases. Figure 8 shows contours of the Reynolds stress for different wave ages. It is apparent that the Reynolds stress distribution is strongly dependent on wave phase and this dependence changes drastically with the wave age. For the case of c/u*=2, the maximum of Reynolds stress lies above the wave trough. Besides this apparent peak region, there exists a second high Reynolds stress region that extends from the first to the upward downstream direction over the wave crest. For cases of c/u*=14 and 25, the positive peak moves to the leeside of the crest, while there is a negative peak on the windward side of the crest. Here we use the term windward to denote upstream (in terms of the outer flow) of the wave crest in the frame fixed in space.

As pointed out by Hudson (1993), for turbulence over a stationary wavy wall, there exists a thin region with small negative Reynolds stress on the windward side of the crest. Hudson (1993) attributed this negative Reynolds stress to be an artifact of the Cartesian coordinate system used in the simulation and analysis. However, this argument is inadequate to explain the existence of the negative Reynolds stresses region with large magnitude and large size as shown in Figures 8 (b) and (c). When the water wave is moving fast, the magnitude of the vertical velocity in the air induced by the wave motion is comparable to the mean streamwise velocity of the wind. Similar to the negative correlation between u' and w' in a boundary layer flow with $U(z)$, the wave induced vertical velocity here creates a shear flow $W(x)$ in the vertical direction. The combined effect of $U(z)$ and $W(x)$ results in a positive correlation of u' and w' on the windward side, i.e. a negative Reynolds stress.

A useful tool in the study of Reynolds stress is quadrant analysis. Contribution to the Reynolds stress is divided into four quadrants: Q1 ($u'>0, w'>0$), Q2 ($u'<0, w'>0$), Q3 ($u'<0, w'<0$), and Q4

($u' > 0, w' < 0$). Previous research shows that Q2 and Q4 motions dominate in flat wall boundary layers, which are know as ejection and sweep events, respectively (Kim et al. 1987). However, as shown earlier, for waves with relatively large phase speed, Q2 and Q4 do not necessarily indicate ejections and sweeps. The classification of ejection and sweep depends on local profiles of u and w.

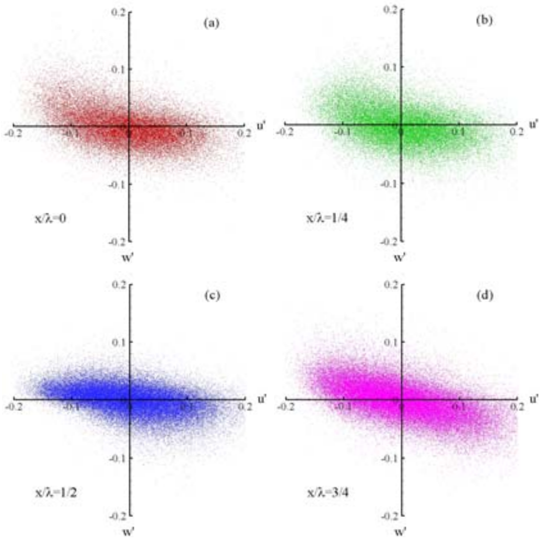

Figure 9: Distribution of (u', w') for the case of (ka, c/u*) = (0.25, 2). Different streamwise locations are chosen: (a) above windward side; (b) above crest; (c) above leeward side; and (d) above trough.

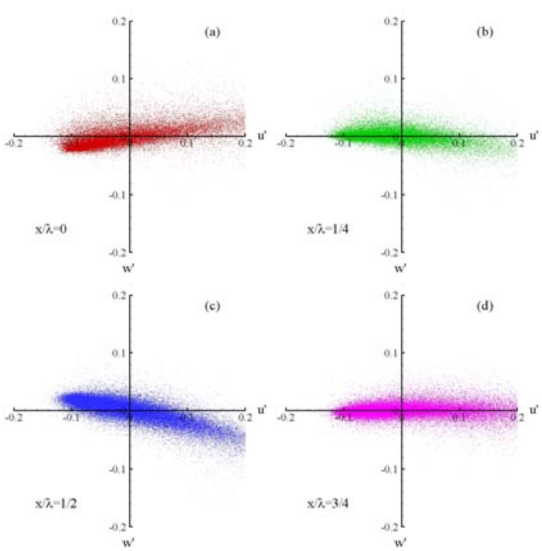

Figure 10: Same as in Figure 9 but for the case of (ka, c/u*) = (0.25, 25).

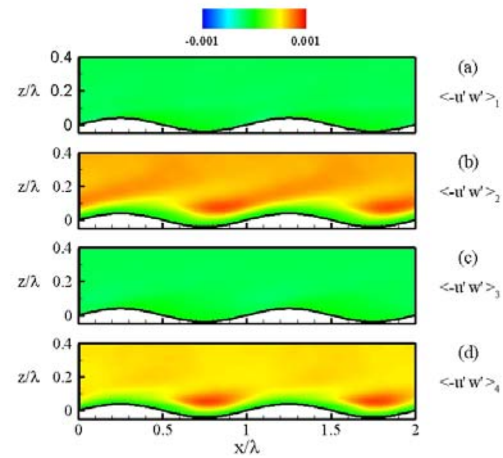

Figure 11: For the case of (ka, c/u*) = (0.25, 2), contributions to Reynolds stress from quadrants: (a) Q1: $u' > 0, w' > 0$; (b) Q2: $u' < 0, w' > 0$; (c) Q3: $u' < 0, w' < 0$; and (d) Q2: $u' > 0, w' < 0$.

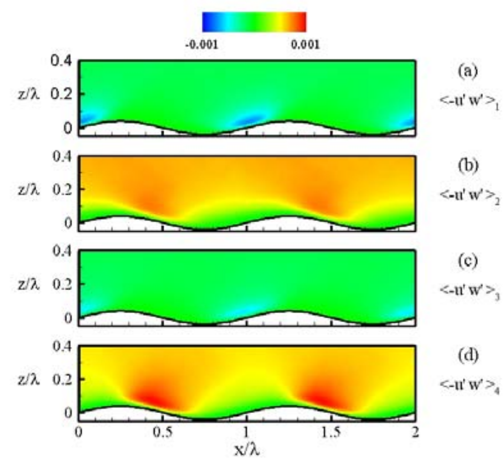

Figure 12: Same as in Figure 11 but for the case of (ka, c/u*) = (0.25, 14).

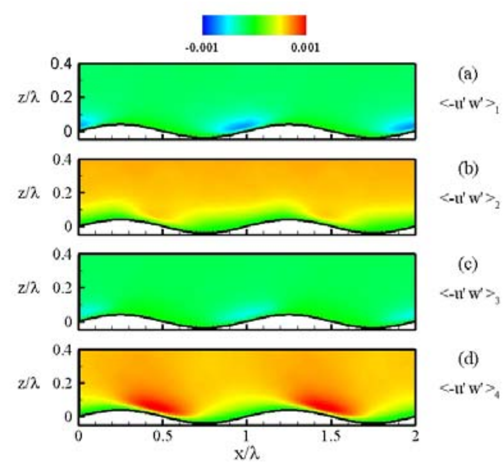

Figure 13: Same as in Figure 11 but for the case of (ka, c/u*) = (0.25, 25).

Figures 9 and 10 show the quadrants of (u', w') at different wave phases for c/u*=2 and 25 at a fixed height above wave surface for different streamwise locations. The c/u*=14 case is similar to c/u*=25 and the results are not shown here. The heights chosen for sampling in both cases are the ons where the peak values of the Reynolds stress are located. For the case of c/u*=2, the quadrants are dominated by Q2 and Q4, similar to the flat wall case. However, for c/u*=25, we find that: (i) above windward side of crest, Q1 and Q3 dominate; (ii) above leeward side of crest, Q2 and Q4 dominate; (iii) above crest and trough, all quadrants have comparable contributions. This result indicates that when wave motion becomes strong, the shear profile of the wave induced vertical velocity becomes as important as the mean streamwise flow.

We next examine contributions from different quadrants to the Reynolds stress. As shown in Figure 11, for the case of c/u*=2, the Q2 and Q4 events are responsible for most of the Reynolds stress. In Figure 11(b), the peak value of Reynolds stress due to Q2 (ejection in this case) starts above the wave trough, extends to the downstream direction, lifts up above the wave crest, and then becomes weak further downstream. In Figure 11(d), the peak value due to Q4 (sweep in this case) is located right above the wave trough. Distributions of the decomposed Reynolds stress are similar for the cases of c/u*=14 and 25, as can be seen in Figures 12 and 13. The Q1 and Q3 events produce negative Reynolds stress on the windward side of the wave crest, while Q2 and Q4 contribute positive Reynolds stress on the windward side of the wave crest.

As found by previous studies on flat wall boundary layers, the ejection and sweep events of turbulence are strongly related to near-wall coherent structures, which we discuss in the next section for turbulence over water waves.

COHERENT VORTEX STRUCTURES NEAR WAVE SURFACE

We perform an extensive study on coherent turbulence structures in the wind field over waves, which play an important role in wind force on ship superstructures. Previous studies of turbulence over a flat wall have indicated the existence and dynamic importance of coherent vortex structures both experimentally (e.g., Adrian et al. 2000) and numerically (e.g., Kim 1983, Moin and Kim 1985, Kim and Moin 1986, Heist et al. 2000). Based on experimental and numerical observations, many conceptual models for near-wall coherent turbulent structures have been proposed, among which the quasi-streamwise vortex model (e.g., Jeong et al. 1997) and the horseshoe vortex model (e.g., Zhou et al. 1999) are the most widely studied. A comprehensive review of coherent vortical structures in turbulence study can be found in Robinson (1991). For turbulence over wavy surfaces, however, there is a lack of study on coherent vortex structures. The few existing studies are all for stationary wavy walls (e.g. De Angelis et al. 1997, Calhoun and Street 2001, and Tseng and Ferziger 2004). In this study, we employ various identification schemes to visualize instantaneous coherent vortex structures near water wave surfaces. These vortices are then studied statistically by means of conditional averaging.

For the study of coherent vortical structures in turbulence, many identification techniques have been developed for the visualization of vortices. Among those, the vortex line method (Moin and Kim 1985), Q method (Hunt et al. 1988), Δ method (Chong et al. 1990), and λ_2 method (Jeong and Hussain 1995) are the most popular ones. Recently, a new method based on the swirling strength (λ_{ci}) criterion has been developed by Zhou et al. (1999), which was later modified by Chakraborty et al. (2005) by adding another criterion $\lambda_{cr}/\lambda_{ci}$ (hereinafter referred to as the λ_{ci} method). We have employed the above approaches and found both the λ_2 and λ_{ci} methods provide satisfying results in capturing the general topologies of the vortices near wave surfaces, with slight difference in background noise. Without losing generalization, we use the λ_2 method for vortex identification in this paper.

In the λ_2 method, following Jeong and Hussain (1995), we calculate the eigenvalue of the tensor $\mathbf{S}^2+\mathbf{\Omega}^2$, where $\mathbf{S}$ and $\mathbf{\Omega}$ are respectively the symmetric and antisymmetric parts of the velocity gradient tensor $\nabla\mathbf{u}$. Let λ_2 be the second largest eigenvalue of $\mathbf{S}^2+\mathbf{\Omega}^2$, the region where $\lambda_2<0$ defines the interior of a vortex core.

In Figure 14 we plot the instantaneous coherent vortical structures in the near-surface region for young/slow (c/u*=2) and mature/fast (c/u*=25) water waves. It is apparent that the dominant vortex structures near the wave surface are stretched in the streamwise direction for both cases. By comparing Figures 14(a) and (b), it is interesting to see that features of the coherent vortices strongly depend on the wave age c/u*. In the mature wave case, there are vortex sheets lying right above the wave crests and troughs. Detailed investigation (not shown here) indicates that these vortex sheets have vorticity vectors pointing in the spanwise direction. Above the crest, the spanwise vorticity has $\omega_y<0$, while above the trough it has $\omega_y > 0$. This sign distribution suggests that the spanwise vortex sheet is generated by the fast moving wave.

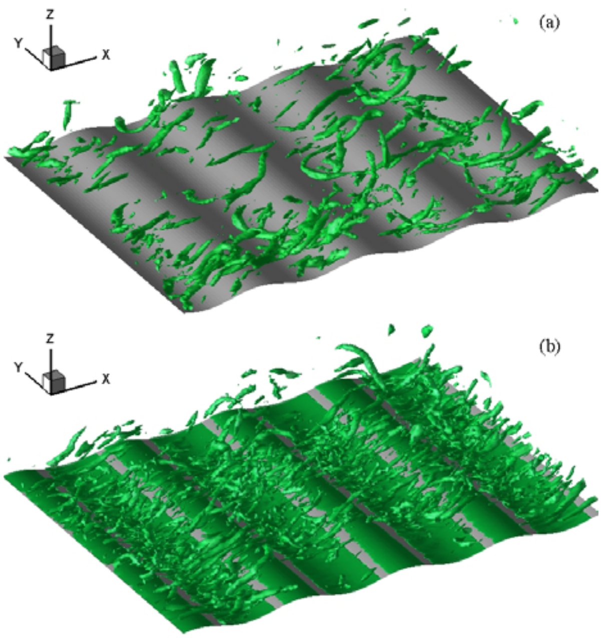

Figure 14: Snapshots of near-wall coherent vortical structures in instantaneous turbulence field over water waves with wave ages: (a) c/u*=2; and (b) c/u*=25.

Figure 15 shows a top view of the instantaneous flow field as shown in Figure 14(a). The background shade and the blue curve at the bottom of the figure denote the wave surface displacement. Vortices with positive streamwise vorticity are colored by blue, while those with negative streamwise vorticity are yellow. Several typical coherent vortex structures are marked with numbers 1 to 6. Vortices number 1 and 3 are quasi-streamwise vortices with positive ω_x, while vortex number 2 is a quasi-streamwise vortex with negative ω_x. As shown in the figure, these quasi-streamwise vortex structures start from the windward side of a wave crest, and they extend over the wave crest. Another type of vortex structures is the horseshoe vortex, e.g. vortices number 4 to 6 in Figure 15. It is a little surprising that these horseshoe vortices have their head upstream but legs downstream. This is the opposite of the typical horseshoe vortices near a flat wall, of which the heads are downstream of the legs. Also we found that the heads of these vortices are usually located above the wave trough. Generally speaking, the quasi-streamwise structures are dominant near the surface. The horseshoe vortices, together with some arch vortices and some small spanwise vortices, concentrate near the wave trough.

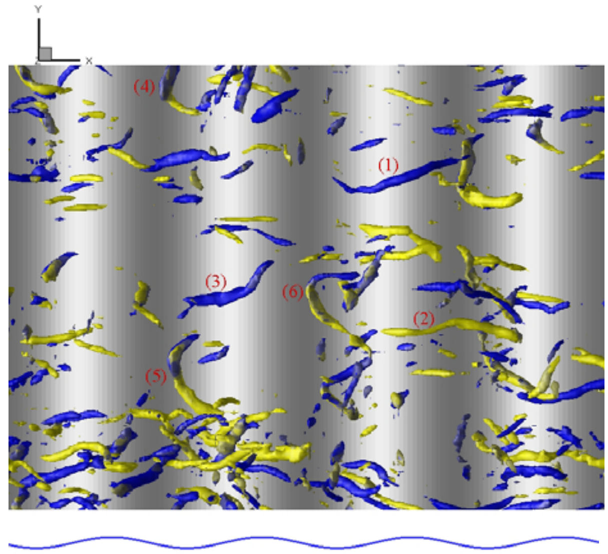

Figure 15: Top view of instantaneous vortices shown in Figure 14(a). Structures with blue color are vortices with positive streamwise vorticity; those with yellow are vortices with negative streamwise vorticity. Typical coherent vortex structures are marked with numbers from 1 to 6.

In order to study the dependence of vortex distribution on wave ages, we calculate the conditionally phase-averaged value of λ_2. Since only the region of $\lambda_2 < 0$ is inside the vortex core, we define a detection function as

$$D(x,y,z,t) = \begin{cases} 1 & \text{if } \lambda_2(x,y,z,t) \le 0 \\ 0 & \text{otherwise} \end{cases}, \qquad (17)$$

and then we calculate the phase-averaged value of the product $D \cdot \lambda_2$. To further decompose the contribution from quasi-streawise and spanwise vortices, we apply another conditional function

$$E(x,y,z,t) = \begin{cases} 1 & \text{if } \sqrt{\omega_x^2 + \omega_z^2} > |\omega_y| \\ 0 & \text{otherwise} \end{cases}. \qquad (18)$$

Finally, phase-averaging is performed for the quantity $D \cdot E \cdot \lambda_2$, which is used as an effective indicator for the spatial frequency of quasi-streamwise vortex occurrence.

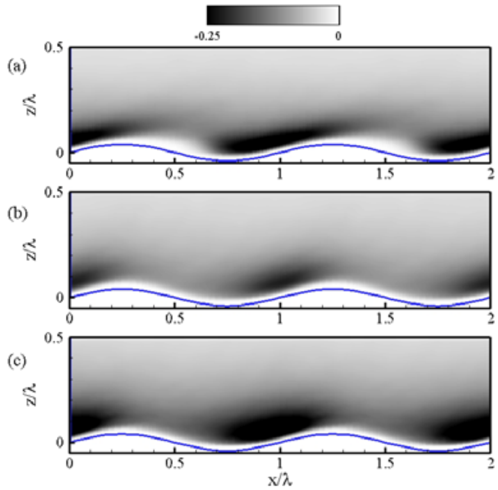

Figure 16: Phase-averaged contours of $D \cdot E \cdot \lambda_2$ for turbulence over plane progressive waves with steepness ka=0.25 and wave ages of: (a) c/u*=2; (b) c/u*=14; and (c) c/u*=25.

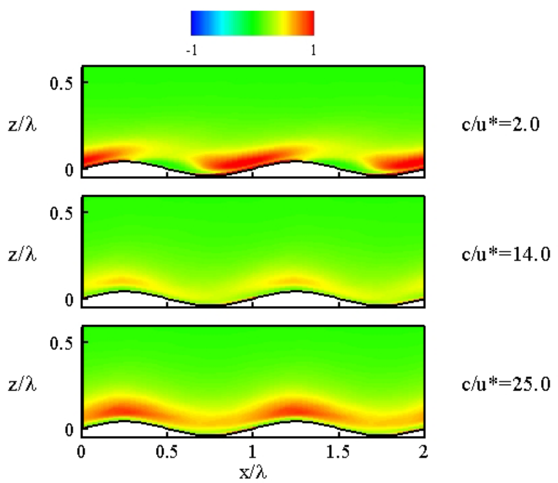

Figure 17: Phase-averaged contours of enstrophy component $\langle \omega_x' \omega_x' \rangle$ for cases c/u*=2, 14, and 25.

Figure 16 shows the phase-averaged contours of $D \cdot E \cdot \lambda_2$ for the cases of c/u*=2, 14, and 25. For the c/u*=2 case, the quasi-streamwise vortices have the maximum concentration on the windward side of the wave crest. The vortices start from the trough, extend to the downstream direction, lift up above the crest, and then become weak above the leeside of the crest. This variation is very similar to the distribution of Reynolds stress due to Q2 event as shown in Figure 11(b). This similarity suggests that for the young wave case c/u*=2, ejection events on the windward side of the wave crest are induced by quasi-streamwise vortices.

For the cases of c/u*=14 and 25, the quasi-streamwise vortices also concentrate on the windward side of the crest. The c/u*=14 case has lower peak value than the c/u*=25 case, indicating that the quasi-streamwise vortices in the intermediate waves occur less frequently than in mature waves.

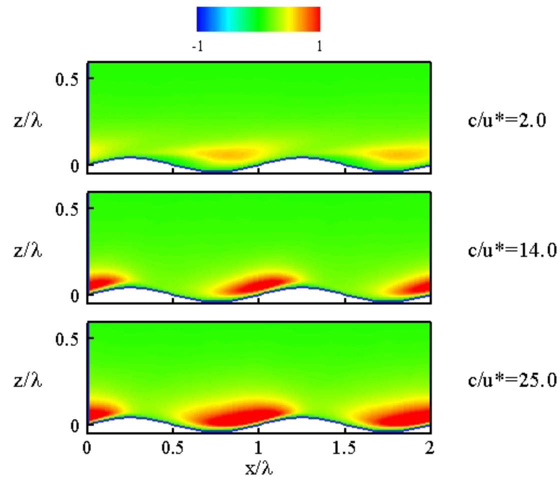

Figure 18: Same as in Figure 17 but for enstrophy component $\langle \omega_z' \omega_z' \rangle$.

Because the contours in Figure 16 do not tell the direction of the vortices in x-z plane, we further calculate the phase-average value of the enstrophy component $\langle \omega_i' \omega_i' \rangle$. The results are shown in Figures 17 and 18. By comparing with Figure 16, we find that due to the slope of the wave surface, the quasi-streamwise vortices are inclined to the vertical direction near the trough, while turning to the streamwise direction above the crest. Comparing with Figure 14(b), we can see that the vortices riding above the wave crest tend to bend to follow the slope of the wave crest.

EDUCED VORTEX STRUCTURES

In this section, we use another conditional average approach to educe characteristic coherent structures in the wind field above water waves. Compared with the flat wall case, turbulent flows over waves have several complex features including streamwise variation of the surface slope, wave orbital velocity, streamwise pressure gradient, and propagation of wave form. These additional characteristics introduce streamwise variations and topology changes to vortex structures. As such, our experience shows that it is often difficult to apply existing conditional average schemes such as the Reynolds-stress based variable-interval special-averaging (VISA) method (Kim 1983) in the present wind-over-wave problem.

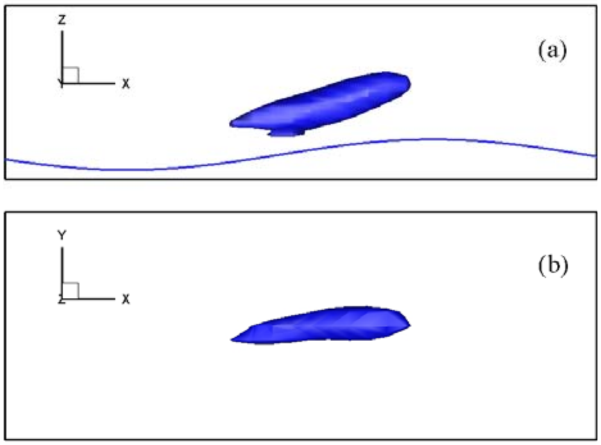

Figure 19: Educed quasi-streamwise vortex with positive streamwise vorticity by means of conditional average: (a) side view; (b) top view. The blue curve represents conditional-averaged wave surface.

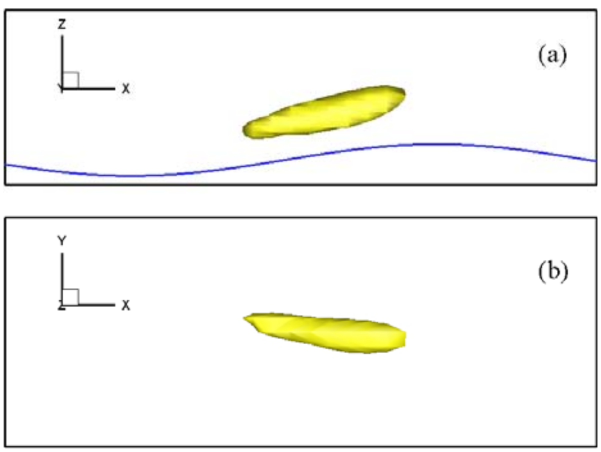

Figure 20: Same as in Figure 19 but for vortices with negative streamwise vorticity.

To overcome this difficulty, we develop a new conditional average scheme. In our approach, the variable-interval function is based on the λ_2 value rather than the Reynolds stress. After the local extrema of the variable-interval function are found, we further search the spatial points in the neighbourhood to obtain geometry characteristics of the vortex structure. Finally, the vortices to be sampled for the conditional averaging are determined based on the vortex topology. We find this new approach can faithfully capture vortex structures in question.

Figures 19 and 20 show the educed quasi-streamwise vortices with positive and negative streamwise vorticity, respectively, for the young wave case c/u*=2. It is shown that quasi-streamwise vortices are located above the windward side of the wave crest, consistent with Figure 16(a). By comparing Figure 19(b) with Figure 20(b), we find that when extending to the downstream direction, the educed positive quasi-streamwise vortex inclines slightly to the left, while the negative quasi-streamwise vortex inclines to the right.

As pointed out by Kim and Moin (1986), when a Reynolds stress based VISA scheme is used, the conditionally averaged structures are smeared out relative to the instantaneous ones, and care should be taken when they are used to model instantaneous structures. In the present study, we use the value of λ_2 to extract vortical structures from the surrounding fluid, of which the topology is further checked. Only those belong to the specific vortex type that we are looking for are taken as samples for averaging. Therefore, the educed structures by our approach are more related to the instantaneous ones than those educed by the conventional VISA scheme.

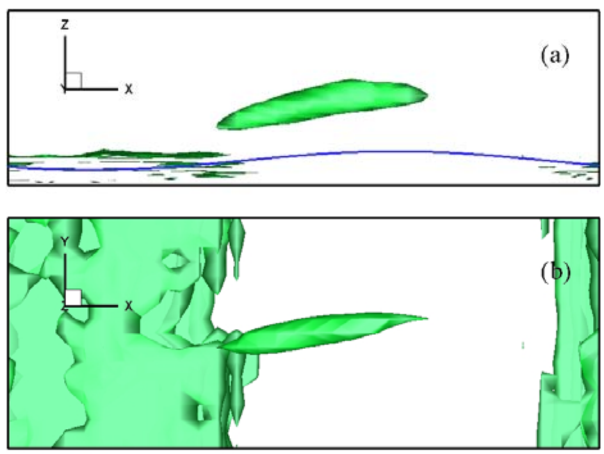

Figure 21: Same as in Figure 19 but for the case of c/u*=14.

The educed quasi-streamwise vortices for cases of c/u*=14 and 25 are shown in Figures 21 and 22, respectively. Due to space limitation, we only present results for quasi-streamwise vortices with positive ω_x here. The structures near the wave crest and trough are due to the spanwise vortex sheets generated by strong wave motion, as shown in Figure 16(b). As pointed out earlier, these spanwise vortices are wave phase coherent (that is, $\omega_y < 0$ above crest and $\omega_y > 0$ above trough) and they are distributed along the spanwise direction. Unlike other structures that occur stochastically, these spanwise vortical structures survive the conditional averaging procedure and they are evident in the educed field. Similar to the case of c/u*=2, the positive quasi-streamwise vortices incline to left as they extend to the downstream direction. However, for the intermediate and mature waves, these vortices are located further downstream compared to the young wave case, again in consistence with the statistical results shown in Figure 16.

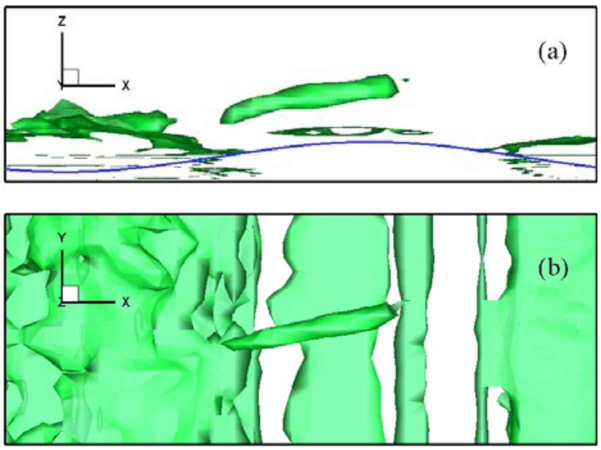

Figure 22: Same as in Figure 19 but for the case c/u*=25.

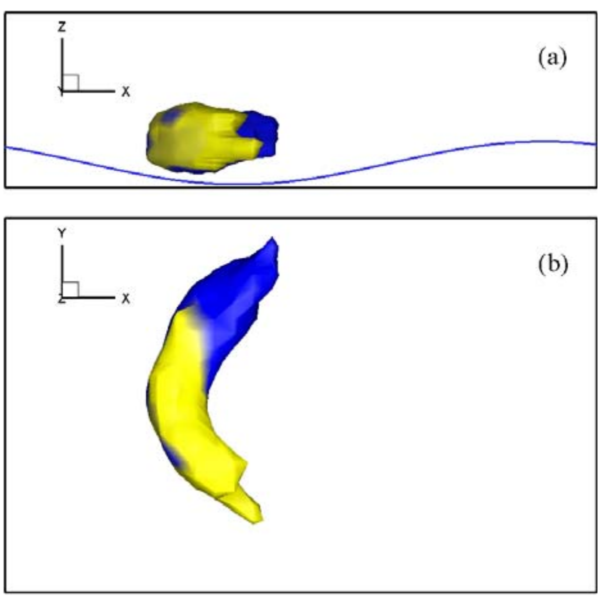

Figure 23: Educed arch vortex for the case of c/u*=2 by means of conditional average: (a) side view; (b) top view. The blue curve represents conditionally-averaged wave surface.

As shown earlier, there also exist horseshoe vortices near the wave trough. We also apply the conditional average method to educe this type of vortices. Figure 23 shows that the educed horseshoe vortex is located slightly upstream of the wave trough. The arch shape head of the horseshoe vortex is clearly shown in the figure. The beginnings of the two legs are indicated by the blue and yellow colors corresponding to positive and negative streamwise vorticity, respectively. As shown in Figure 15, each individual horseshoe vortex may have quite different shapes including different angles and different distances between the two legs. This spatial variation results in the smearing out of the two legs during the averaging procedure. Therefore, instead of a complete horseshoe shaped vortex, we obtain an arch vortex as shown in Figure 23(b).

Recalling that in Figure 11(d), the Reynolds stress due to the Q4 (sweep) event has its peak above the wave trough. Around the same location, there exist horseshoe vortices, arch vortices, and small spanwise vortices, (hereinafter, they are all named as arch family of vortices), as shown in Figures 15 and 23. These vortices are all associated with downwelling motion (sweeps) of the fluid on the downstream side of their heads. Therefore, this arch family of vortices may also play an important role in turbulence production and dissipation. Now the question is: Is this arch family of vortices caused by the sweep event? Or are they actually generated by other mechanisms, such as mean shear induced instability, and do they in turn cause sweep motion? The answer is not clear yet, and further investigation is needed.

PRESSURE IN WIND FIELD

Another important question is how the pressure varies in wind-wave interactions. Such information is essential to the wind force on ship superstructures. It also plays an important role in the study of effects of wind input on deterministic prediction of wave propagation. For this purpose, we investigate pressure statistics in wind-wave interactions.

Figure 24 shows the phase-averaged wave-correlated pressure contours of winds over plane progressive waves with wave ages c/u*=2 and 14. It is found that, for the young wave case of c/u*=2, the pressure contours are tilted at a short distance above the wave. For the intermediate wave with c/u*=14, the high pressure region does not extend vertically much comparing to the wave amplitude. It is found that the young wave is substantially affected by the wind-induced surface drift. With the presence of a wind-generated surface drift, the low pressure region is shifted towards the trough, while the high pressure region is extended slightly in the downstream direction. Effect of surface drift on the pressure field for the intermediate wave is less obvious.

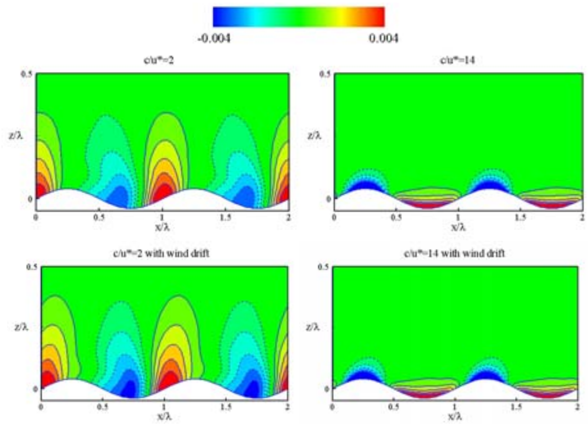

Figure 24: Phase-averaged wave-correlated pressure contours for surface waves with wave ages c/u*=2 and 14. In the two lower figures, the wind-generated surface drift is considered.

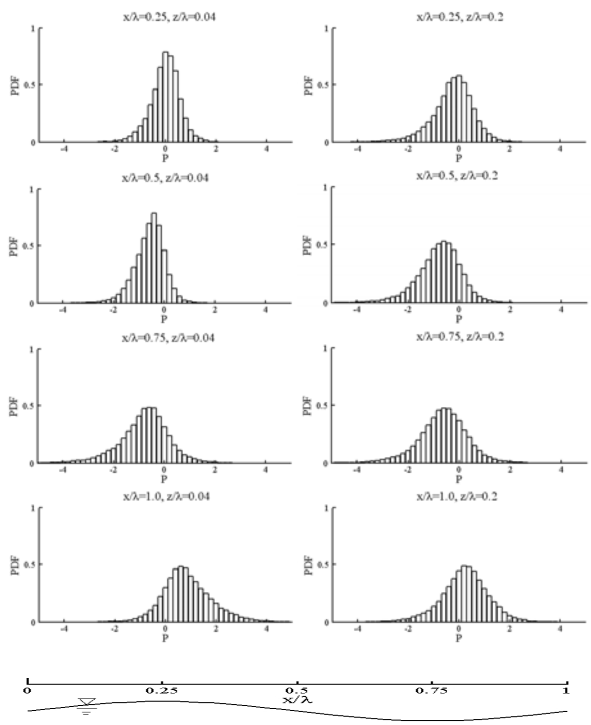

Figure 25: Histograms of pressure distribution probability at different locations for wind over water wave. Wave age is c/u*=2. Here, the pressure is normalized by the root-mean-square of the surface pressure fluctuation.

From the above observation, it is clear that the pressure field distribution is a strong function of wave phase, which may play an important role in the wind load on ships when the ship length is comparable to the wavelength of the dominant wave. The pressure may vary significantly in the vertical direction near the water surface, and its spatial variation is highly dependent on the wave age, signifying the importance of wind-wave dynamical interaction.

While Figure 24 presents the averaged result of wind pressure, it is also important to consider the fluctuations of the wind pressure. Such gust effect may be essential for the investigation of ship motions and wind loads. For this purpose, we investigate the probability density distribution of the pressure. It is found that young waves have wider pressure distributions, i.e. more variations, than mature waves (results not shown here due to space limitation). To illustrate the spatial distribution of pressure fluctuations, we plot in Figure 25 histograms of pressure distribution at two different heights above the wave. It is shown that at the leeside and at the trough, the pressure obtained at some distance above has more fluctuations than the wind input at the wave surface. Such effects may affect the structural dynamics of the ship in respond to wind load.

EVOLUTION OF COMPLEX BROADBAND WAVEFIELD INTERACTING WITH WIND

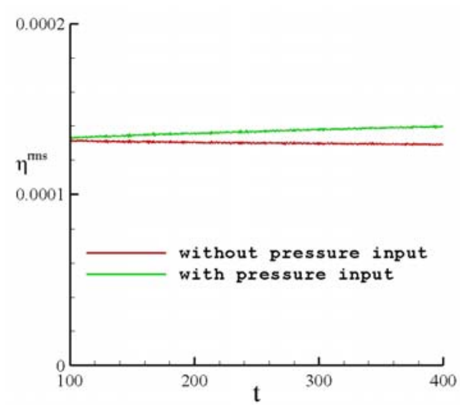

Figure 26: Time history of the root-mean-square of wave surface displacement.

In order to study the effect of wind input on ocean wavefield evolution, we utilize our coupled wind-wave code to simulate broadband wind-wave field. For comparison, we perform two parallel computations with one-way and two-way coupling, respectively: (i) the wave surface motion is used as a boundary condition for the turbulence simulation, but the turbulence pressure is not applied to the wave simulation (in other words, p_a is set to be zero in the dynamic boundary condition for wave simulation); and (ii) exact coupling as described earlier. We start the two simulations with identical initial conditions from a JONSWAP ocean wave spectrum (Hasselmann et al. 1973). Instantaneous flow fields are illustrated in Figure 4 to 6.

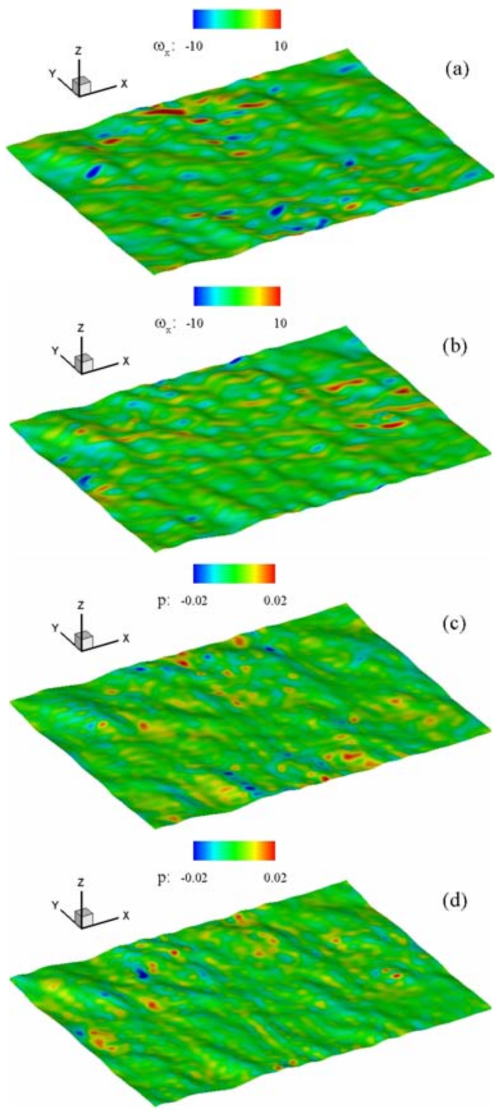

Figure 27: Comparison of surface contours without (Figures (a) and (c)) and with (Figures (b) and (d)) wind input from air to wave. Contours in (a) and (b) are for streamwise vorticity of air on the wave surface. Contours in (c) and (d) are air pressure acting on the wave surface.

Figure 26 shows the time history of the root-mean-square of wave surface displacement from simulations (i) and (ii). Apparently, when the two-way coupling between wind turbulence and waves is captured in the simulation, the wave obtains energy input from the wind by work of the air pressure, and the wave grows with time.

Figure 27 shows comparison of streamwise vorticity and air pressure at the wave surface between the two simulations. It is found that one-way and two-way coupling can have appreciable differences in the results, especially for the surface pressure distributions. We remark that the results in Figures 26 and 27 are for low wind conditions (the wind speed at 10 meters above sea level is 6.8m/s). One can imagine that for high winds, one-way and two-way coupling simulations can lead to wavefields that are substantially different. The one-way coupling simulation for wind turbulence over water waves, which employs prescribed wave boundary conditions, may not be able to make accurate predictions of wind-wave evolution. The two-way coupling simulation tool we develop in the present study, on the other hand, overcomes this shortcoming. Due to the high efficiency of the HOS method, the two-way coupling increases the computational cost only slightly compared to the one-way coupling.

Figure 28 shows a comparison between instantaneous pressure and vortex structures in the wind turbulence over the JONSWAP wavefield obtained from the two-way coupling simulation. Here the pressure structures are identified by the iso-surface of the negative pressure value p=-0.007, and the snapshot is taken at the same instantaneous time as in Figure 6. By comparison with vortex structures, we find that the pressure structures have much larger vertical extension and they can be connected to the wave surface. A close-up view for the sub-domain marked by the black frame in Figure 28(a) is shown in Figure 28(b)-(e). It is apparent that there exists a strong correlation between the coherent vortex structures and the pressure structures.

As shown earlier, the water wave can have strong influence on the distribution of near-surface coherent vortices in the wind. As a result, strong influence of the water wave on the air pressure is expected. This is confirmed by the results in Figure 27. Comparing to one-way coupling, the two-way coupling simulation has a quite different distribution of coherent vortices in the wind turbulence and hence a different wind pressure distribution. Since the near-surface wind pressure plays an important role in the estimation of wind loads on ship as well as in the prediction of wave evolution under wind excitation, we remark that a two-way coupling simulation is necessary.

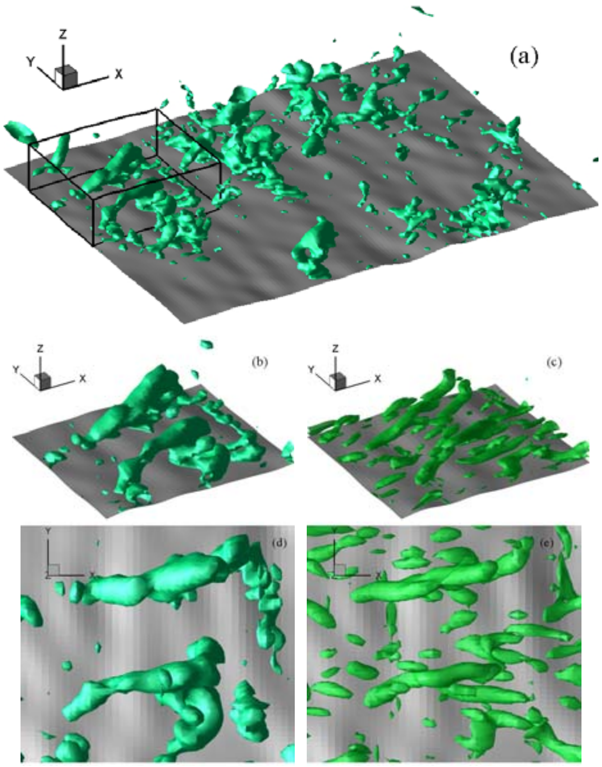

Figure 28: Correlation between the instantaneous pressure and vortex structures in wind turbulence over JONSWAP wavefield. The same snapshot as Figure 6 is chosen and the pressure structures identified by the iso-surface of p=-0.007 is shown in (a). A subzone in figure (a) indicated by a black frame is extracted for detailed comparison: (b) and (c) are the side views of pressure and vortex structures, respectively; (d) and (e) are the top views of the pressure and vortex structures, respectively.

CONCLUSIONS AND DISCUSSION

In this study, we develop a novel numerical capability for wind and wave simulation for naval applications. The wavefield is computed with an efficacious high-order spectral (HOS) method that directly captures key nonlinear wave interaction processes, with the phases of all the dynamically important wave components being resolved. With wind turbulence simulation and kinematic and dynamic coupling at the sea surface, we are able to simulate ocean wave and wind evolution and their interaction in a direct, phase-resolved physical context for the first time.

Equipped with the computational capability developed above, we perform a systematic study on the wind turbulence over broadband ocean wavefields and plane progressive waves with a wide range of environmental parameters. In this paper, we discuss representative results on flow structures, statistics of momentum transport, coherent vortices, and wind pressure, which are found strongly dependent on the wavefield. We also show that the wind may have significant effects on wave evolution. Therefore, the dynamic coupling between the wind and the waves may be essential for many of the Navy's applications, and the unique numerical tool developed in our work provides a powerful tool for the study of wind-wave interactions.

Computation of phase-resolved surface wavefield and marine atmospheric boundary layer may lead to better understanding and prediction of the ocean environment for naval ship operation and maneuvering. Together with data assimilation techniques and multiscale modeling, we aim to provide the Navy with a new powerful tool to predict nonlinear, large wavefield with finely-resolved temporal and spatial detail. The new phase-resolved, deterministic tool is fundamentally different from existing phase-averaged, statistical wave modeling tools, with the potential of being able to make more accurate prediction because of its direct, physics-based approach.

The coupled wind-wave simulation capability can also be used as a tool for naval ship design and operation when wind forcing on the superstructures is of concern. To estimate wind loads, it is essential to understand the wind turbulence field including both the mean and the stochastic quantities (Simiu and Scanlan 1996, Liu 1991). Systematic simulation of winds over ocean waves under various sea conditions provides valuable database in the design and test circle. Together with ship hydrodynamics simulations, computation for surface ship operations under high wind and severe wave conditions is one of our long-term goals of research.

ACKNOWLEDGEMENT

This research was financially supported by ONR. Most of the computations were performed with the computing resources provided by the DoD HPC Modernization Program.

REFERENCES

[1] Wu, G., Liu, Y. and Yue, D.K.P., "Studying rogue waves using large-scale direct phase-resolved simulations," Proc. 14th 'Aha Huliko' a Hawaiian Winter Workshop on Rogue Waves, 2005.

[2] Dommermuth, D.G. and Yue, D.K.P., "A high-order spectral method for the study of nonlinear gravity waves." J. Fluid Mech., Vol. 184, 1987, pp. 267-288.

[3] Sullivan, P.P., McWilliams, J.C. and Moeng, C.-H., "Simulation of turbulent flow over idealized water waves." J. Fluid Mech., Vol. 404, 2000, pp. 47-85.

[4] Shen, L., Zhang, X., Triantafyllou, M.S., and Yue, D.K.P., "Turbulent flow over a flexible wall undergoing a streamwise travelling wave motion," J. Fluid Mech., Vol. 484, 2003, pp. 197-221.

[5] Dimas, A.A. and Fialkowski, L.T. "Large-wave simulation (LWS) of free-surface flows developing weak spilling breaking waves." J. Comput. Phys.,Vol. 159, 2000, pp.172-196.

[6] Shen, L. and Yue, D.K.P., "Large-eddy simulation of free-surface turbulence," J. Fluid Mech., Vol. 440, 2001, pp. 75-116.

[7] Shen, L., "Physics of free-surface turbulence and challenges to LES," Monography: CFD of Multifluid Flows., Published by von Karman Institute for Fluid Dynamics, 2007.

[8] Shen, L. and Yue, D.K.P., "Modeling the relationships between flow statistics and structures at the coupled air-ocean interface," Oceanography, Vol. 19, 2006, pp. 52-63.

[9] Liu, S., Shen, L. and Yue, D.K.P., "Numerical investigation of coupled air-water turbulent boundary layers," 2008, in review.

[10] Harlow, F.H. and Welch, J.E., "Numerical calculation of time-dependent viscous incompressible flow of fluid with free surface," Phys. Fluids, Vol. 8, 1965, pp. 2182-2189.

[11] Kim, J. and Moin, P., "Application of a Fractional-Step Method to Incompressible Navier-Stokes Equations," J. Comput. Phys., Vol. 59, 1985, pp. 308-323.

[12] Zakharov, V.E., "Stability of periodic wave of finite amplitude on the surface of a deep fluid," J. Appl. Mech. Tech. Phys., Vol. 2, 1968, pp. 190-194.

[13] Mei, C.C., Stiassnie, M., and Yue, D.K.P., Theory and applications of ocean surface waves, Part 2, 2nd ed., World Scientific, New Jersey, 2005, pp. 888-902.

[14] Lombardi, P., De Angelis, V., and Banerjee, S., "Direct numerical simulation of near-interface turbulence in coupled gas-liquid flow," Phys. Fluids, Vol. 8, 1996, pp. 1643-1665.

[15] Hasselmann, K., Barnett, T.P., Bouws, E., Carlson, H., Cartwright, D.E., Enke, K., Ewing, J.A., Gienapp, H., Hasselmann, D.E., Kruseman, P., Meerburg, A., Muller, P., Olbers, D.J., Richter, K., Sell, W., Walden, H., "Measurements of wind-wave growth and swell decay during the Joint North Sea Wave Project (JONSWAP)," Deutsches Hydrographisches Institut, Hamburg, UDC 551.466.31; ANE German Bight, 1973.

[16] Belcher, S.E. and Hunt, J.C.R., "Turbulent flow over hills and waves," Ann. Rev. Fluid Mech., Vol. 30, 1998, pp. 507-538.

[17] Miles, J.W., "On the generation of surface waves by shear flows," J. Fluid Mech., Vol. 3, 1957, pp. 185-204.

[18] Lighthill, M.J., "Physical interpretation of the mathematical theory of wave generation by wind," J. Fluid Mech., Vol. 14, 1962, pp. 385-398.

[19] Hudson, J.D., "The effect of a wavy boundary on a turbulent flow," PhD thesis, University of Illinois, 1993.

[20] Kim, J., Moin, P., and Moser, R., "Turbulence statistics in fully developed channel flow at low Reynolds number," J. Fluid Mech., Vol. 177, 1987, pp. 133-166.

[21] Adrian, R. J., Meinhart, C.D., and Tomkins, C.D., "Vortex organization in the outer region of the turbulent boundary layer," J. Fluid Mech., Vol. 422, 2000, pp. 1-54.

[22] Kim, J., "On the structure of wall-bounded turbulent flows," Phys. Fluids, Vol. 26, 1983, pp. 2088-2097.

[23] Moin, P. and Kim, J., "The structure of the vorticity field in turbulent channel flow. Part 1. Analysis of instantaneous fields and statistical correlations," J. Fluid Mech., Vol. 155, 1985, pp. 441-464.

[24] Kim, J. and Moin, P., "The structure of the vorticity field in turbulent channel flow. Part 2. Study of ensemble-averaged fields," J. Fluid Mech., Vol. 162, 1986, pp. 339-363.

[25] Heist, D.K., Hanratty, T.J., and Na, Y., "Observations of the formation of streamwise vortices by rotation of arch vortices," Phys. Fluids, Vol. 12, 2000, pp. 2965-2975.

[26] Jeong, J., Hussain, F., Schoppa, W., and Kim, J., "Coherent structures near the wall in a turbulent channel flow," J. Fluid Mech., Vol. 332, 1997, pp. 185-214.

[27] Zhou, J., Adrian, R.J., Balachandar, S., and Kendall, T.M., "Mechanisms for generating coherent packets of hairpin vortices in channel flow," J. Fluid Mech., Vol. 387, 1999, pp. 353-396.

[28] Robinson, S.K., "Coherent motions in the turbulent boundary layer," Ann. Rev. Fluid Mech., Vol. 23, 1991, pp. 601-639.

[29] De Angelis, V., Lombardi, P., and Banerjee, S., "Direct numerical simulation of turbulent flow over wavy wall," Phys. Fluids, Vol. 9, 1997, pp. 2429-2442.

[30] Calhoun, R.J. and Street, R.J., "Turbulent flow over a wavy surface: Neutral case," J. Geophys. Res., Vol. 106, 2001, pp. 9277-9293.

[31] Tseng, Y.-H. and Ferziger, J.H., "Large-eddy simulation of turbulent wavy boundary flow – illustration of vortex dynamics," J. Turbulence, Vol. 5, 2004, 034.

[32] Hunt, J.C.R., Wray, A.A., and Moin, P., "Eddies, stream, and convergence zones in turbulent flows," Center for Turbulence Research Report CTR-S88, 1988, pp. 193-208.

[33] Chong, M.S., Perry, A.E., and Cantwell, B.J., "A general classification of three-dimensional flow fields," Phys. Fluids A, Vol. 2, 1990, pp. 765-777.

[34] Jeong, J. and Hussain, F., "On the identification of a vortex," J. Fluid Mech., Vol. 285, 1995, pp. 69-94.

[35] Chakraborty, P., Balachandar, S., and Adrian, R.J., "On the relationships between local vortex identification schemes," J. Fluid Mech., Vol. 535, 2005, pp. 189-214.

[36] Simiu, E and Scanlan, R.H., Wind Effects on Structures, Fundamentals and Applications to Design, 3rd ed., Wiley, New York, 1996.

[37] Liu, H., Wind Engineering, 1st ed., Prentice-Hall, New Jersey, 1991.